Active tuning of vibration for periodic piezoelectric micro systems: a non-local Mindlin plate finite element approach

Zixu Xia, Yu Cong, Shuitao Gu, Zhi-Qiang Feng

Active tuning of vibration for periodic piezoelectric micro systems: a non-local Mindlin plate finite element approach

Z. X. Xia [a,b], **Y. Cong** [b*], **S. T. Gu** [a*], **Z.-Q. Feng** [b]

[a] *School of Civil Engineering, Chongqing University, Chongqing 400044, China*
[b] *Université Paris-Saclay, Univ Evry, LMEE, 91020, Evry, France*

Abstract

The present paper is aimed to propose a multi-parameter feedback control method combined with couple stress elasticity to model piezoelectric micro plate coupled systems. The proposed methodology can be used to design controllers for tuning vibration and wave propagation properties of micro scale plates based on coupled piezoelectric sensors and actuators. Specifically, we use a three-parameter relationship that describes the voltage gain within the sensor-to-actuator circuit involving multiple dependence based on mass, damping and stiffness. Consequently, effect of these parameters can be simulated either independently or collectively so as to obtain the optimal control strategy with respect to the required vibroacoustic properties. Meanwhile, since micro plates are involved, the inherent microstructure effects must be accounted for. Hence, the modified couple stress elasto-dynamics is applied and the micro plate model is discretised with a four-node quadrilateral non-conforming element that offers nodal compatibility with high-order theories of elasticity. Based on the proposed numerical methodology, we investigated the feedback control parametrisation for a reference micro plate coupled system which presents significant microstructure effects. Our analysis allowed characterisation of the three control parameters based on their individual effects, and revealed that their combined effect cannot be predicted by considering direct superposition of their individual behaviours. Therefore, the proposed computational methodology provides a convenient solution for the choice and parametrisation of the feedback controller leading to tunable band gap properties of micro scale plate structures.

Keywords: Active tuning; Vibration control; Piezoelectric; Couple stress theory; Band gap analysis

1 Introduction

Active tuning of vibrations in micro scale electromechanical systems can be achieved by employing piezoelectric micro components as sensors and actuators coupled via an external control algorithm that regulates the real-time state of the system, leading to controlled vibration. Recently, with the rapid development of fabrication technologies in miniaturised systems, integration of piezoelectric micro components into micro-to-nano scale devices has led to remarkable applications such as nano oscillators [1] and resonators [2], micro bio-mimetic robots [3], ultrasonic sensing systems [4], etc. Consequently, tuning of vibration properties for micro scale piezoelectric coupled systems has become an important

* Corresponding authors:
yu.cong@univ-evry.fr (Y. Cong)
gust@cqu.edu.cn (S. T. Gu).

Accepted preprint
July 2022

topic. Meanwhile, due to the emergence of microstructure effects, vibroacoustic behaviours of these miniaturised systems are frequently subject to size dependence which makes their design and optimisation a challenging task, both on the aspect of mechanical modelling and on the associated control strategies.

Vibration of piezoelectric coupled systems can be tuned for wavelengths on the length scale of the system's microstructure. Therefore, systems fabricated on the macro scale mainly focus on low-frequency vibrations either for vibration attenuation or for energy harvesting. Meanwhile, since macro scale systems do not present size effect, classical theories of elasto-dynamics can be readily applied to offer accurate predictions. This is confirmed with recent investigations [5, 6, 7, 8, 9, 10], which led to numerical and experimental prototypes based on macro scale beam and plate coupled models. Micro scale piezoelectric systems, on the contrary, are intended for tuning high-frequency acoustic waves, even ultrasonic waves [11, 12, 13]. Furthermore, since the microstructure is designed on length scales usually below millimetre level, size dependence becomes non negligible in assessing the vibroacoustic properties. To incorporate size dependence into the material behaviour, a series of high-order elastic models have been proposed, among which the first investigations can be traced back to the work of Mindlin [14], who initiated the research on strain gradient theory using 16 material scale parameters. Subsequently, Lam et al.[15] reduced the number of material scale parameters and proposed a modified three-parameter strain gradient theory. To further simplify the material scale description, Yang et al.[16] proposed a modified couple stress theory which requires only one material scale parameter. Thanks to its simplicity, many investigations have been performed on the basis of Yang's work. In static analysis, we can cite the development of Mindlin plate finite element based on the modified couple stress theory [17]. Then, in dynamic analysis of band structures, micro scale composite plates have been studied using the modified couple stress theory, first analytically [18], then numerically [19].

Beside the microstructure effects, another important aspect in the design of micro plate vibration coupled system is the choice and optimisation of the control strategy. From a general point of view, vibration control strategies can be divided into two categories: passive control and active control. Passive control refers to techniques that prepare band structures based on microstructure design and material assembly. It has been widely applied [20, 21, 22] in areas requiring vibration attenuations within fixed frequency band. For general applications that require tunable acoustic properties on a broader frequency range, we prefer active feedback control which employs closed circuits of sensing and actuating components. We cite, among recent applications, the development of active control on a T-shaped metamaterial with switchable waveguide [23] and the design of a soft acoustic metamaterial membrane with tunable band behaviours [24], etc. The cited applications require implementing coupled systems of sensors and actuators. During their operation, vibration induced voltage is enhanced by the external circuit before it is fed back to the actuator. The coupled system adjusts in real-time the state of vibroacoustic properties. It is therefore important to carefully design the control method which commonly takes the following forms: The first one, by direct proportional feedback control with $V_a = -g_c V_s$, for which the actuating voltage is a linear function of the sensing voltage, itself is proportional to the displacement measure. The second, by velocity based control [25], with $V_a = -g_b \frac{\partial V_s}{\partial t}$, for which the actuating voltage is proportional to the velocity. Then, the third, via acceleration based control [5], with $V_a = -g_a \frac{\partial^2 V_s}{\partial t^2}$, for which the actuating voltage is function of the acceleration. Within the scope of this work, a general form of feedback control method involving simultaneously the effects of displacement, velocity and acceleration will be studied. The sensor-to-actuator voltage gain can be described based on these three parameters independently or collectively.

In this work, we adopt the modified couple stress elasticity combined with Mindlin plate kinematics to address the microstructure effects of micro plates. Since couple stress elasticity involves second-order derivatives in the weak form of the equilibrium equation, at least C_1 continuous interpolation of nodal

variables is required. In practice, finite element implementation of strick C_1 continuity is not a trivial task. We use in this work an alternative solution which consists in applying a four-node quadrilateral plate element with non-conforming formulation [26]. Although this element is C_1 discontinuous on the inter-element boundary, it preserves nodal C_1 continuity and offers tolerable compatibility with couple stress elasticity. To confirm our choice, we conducted the benchmark patch test [17] which did not reveal geometrical distortion. Concerning the aspect of control strategy, we implement a three-parameter feedback control method with multiple dependence with respect to displacement, velocity and acceleration. Both contributions of single-parameter control and multi-parameter control are investigated. The computational methodology presented here can be used to assist parametrisation of feedback controllers for general purpose. Regarding the vibration modal analysis for band calculation, we applied the state space method combined with Floquet Bloch boundary conditions. Furthermore, we performed dynamic response analysis in frequency domain using transfer functions and the state space method and the result is compared with the band gap predictions.

The content of this article is organised as follows: we present in Section 2 the dynamic equilibrium in weak formulation for the piezoelectric coupled system based on the modified couple stress theory. We address in particular the application of the modified couple stress elasticity into the electromechanical coupling problem. In Section 3, we describe the implementation of the non-conforming four-node quadrilateral plate finite element. Then, in Section 4, the proposed feedback control strategy with multiple dependence is described as well as its implementation details. We present in Section 5, techniques that implement the periodic boundary conditions according to Bloch-Floquet theory, which lead to the unit cell band gap problem. In Section 6, we present three numerical examples that validate the presented work on the following aspects: first, the account for size dependence by the implemented piezoelectric micro plate coupled system, then, the effect of multi-parameter control strategy for which we discuss in detail both the strategies of single parameter control, and multi-parameter control. In the end, we draw conclusion and remarks in Section 7.

2 Piezoelectric micro plate coupled systems: dynamic equations

Band gap behaviours may be subject to size dependence when the problem dimension descends below millimetre level. In the case of piezoelectric micro plate coupled systems, this means that for very small problem sizes, the vibration behaviour becomes sensible to the problem size and cannot be accurately predicted by classical elasto-dynamics. Therefore, a high-order continuum theory, here for instance, the modified couple stress theory is applied.

2.1 Modified couple stress elasto-dynamics applied to piezoelectric micro plate coupled system

The studied piezoelectric micro plate coupled system is composed of a based plate (Ω_e) and periodically distributed piezoelectric sensor and actuator patches (Ω_p). We suppose the structure on the microscopic scale for which emergence of size effects should be considered. The periodic structure can be represented by the unit cell depicted in Fig.(1). We describe geometrical relations of the unit cell with respect to the Cartesian coordinate system (x, y, z) as indicated in Fig.(1b). The xy-plane lies on the mid-plane of the base plate. Regarding the material definition, both Ω_e and Ω_p are modelled as deformable couple stress continuum using the modified couple stress theory of elasto-dynamics. First proposed by Yang

et al. [16], the modified couple stress theory allows predicting microstructure effects based on a single material length scale parameter. In this section, we focus on the modelling of mechanical behaviours of the micro plate system and their coupling with piezoelectric effects. Therefore, dynamic equations involving kinematic description, constitutive relations and the equilibrium equation are described.

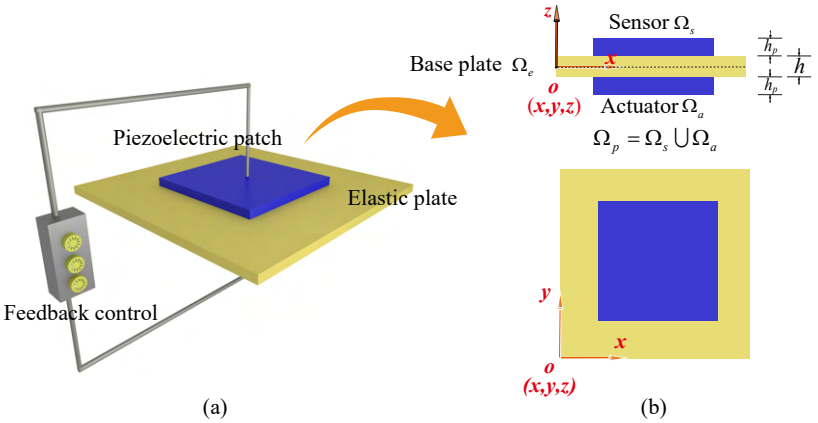

Figure 1: (a) Piezoelectric micro plate coupled system. (b) Periodic unit cell and its geometry described in the Cartesian coordinate system (x, y, z). We use Ω_e to denote the base plate and Ω_p the piezoelectric patches. Sensors and actuators are noted by Ω_s and Ω_a, respectively, thus, $\Omega_p = \Omega_s \cup \Omega_a$. Ω_s and Ω_a are of identical thickness h_p. Thickness of Ω_e is h .

Basic relations

We model Ω_e and Ω_p as deformable couple stress continuum and consider the effect of piezoelectricity only on Ω_p. Therefore, the Gibbs free energy G which involves both the strain energy of $\Omega_e \cup \Omega_p$ and the piezoelectric effects on Ω_p, can be written as

$$\begin{aligned} G = \quad & U_e + U_p \\ = \quad & \frac{1}{2}\int_{\Omega_e} (\boldsymbol{\sigma} : \boldsymbol{\varepsilon} + \boldsymbol{m} : \boldsymbol{\chi})\, \mathrm{d}\Omega \\ & + \frac{1}{2}\int_{\Omega_p} (\boldsymbol{\sigma} : \boldsymbol{\varepsilon} - \mathbf{D}\cdot\mathbf{E} + \mathbf{m} : \boldsymbol{\chi})\, \mathrm{d}\Omega \quad , \end{aligned} \tag{1}$$

where $\mathrm{d}\Omega$ is the unit volume. $\boldsymbol{\sigma}$ and $\boldsymbol{m}$ are Cauchy stress and deviatoric couple stress tensors. Then accordingly, $\boldsymbol{\varepsilon}$ and $\boldsymbol{\chi}$ refer to Cauchy strain and symmetric curvature which can be written as

$$\begin{cases} \boldsymbol{\varepsilon} = \dfrac{1}{2}\left(\nabla \boldsymbol{u} + (\nabla \boldsymbol{u})^T\right) \\ \boldsymbol{\chi} = \dfrac{1}{2}\left(\nabla \boldsymbol{\theta} + (\nabla \boldsymbol{\theta})^T\right) \end{cases} \quad \text{on} \quad \Omega_e \cup \Omega_p \ , \tag{2}$$

where $\boldsymbol{u}$ is the displacement vector and $\boldsymbol{\theta}$ the rotation vector defined by

$$\boldsymbol{\theta} = \frac{1}{2}\nabla \times \boldsymbol{u} \ , \tag{3}$$

in which ∇ denotes Hamiltonian operator and "$\times$" cross product symbol. Eq.(2) applies to kinematics of both the base plate and the piezoelectric patches. To describe the electric field of the piezoelectric

patches, we use $\mathbf{D}$ and $\mathbf{E}$ to denote the electric displacement and the static electric field which derives from the electric potential φ as

$$\mathbf{E} = -\text{grad}\varphi \, . \tag{4}$$

Then, by considering piezoelectric actuator and sensor patches of the same thickness h_p, the voltage V_a and V_s measured on the actuators and sensors in the thickness direction, we can express the actuator and sensor electric field components as

$$\{(E_a)_i\} = \begin{bmatrix} 0 & 0 & \dfrac{V_a}{h_p} \end{bmatrix}^T \quad \text{and} \quad \{(E_s)_i\} = \begin{bmatrix} 0 & 0 & \dfrac{V_s}{h_p} \end{bmatrix}^T . \tag{5}$$

We consider that both piezoelectric patches for sensors and actuators are identical in geometry and material.

Constitutive relations involving elastic-piezoelectric coupling

We distinguish constitutive relations of the base plate and those of the piezoelectric patches that serve as actuators and sensors. For the base plate (Ω_e), linear material behaviours based on couple stress elasticity is considered. Hence, Cauchy stress $\boldsymbol{\sigma}$ and deviatoric couple stress $\boldsymbol{m}$ tensors are expressed as linear functions of Cauchy strain $\boldsymbol{\varepsilon}$ and symmetric curvature $\boldsymbol{\chi}$ tensors

$$\begin{cases} \boldsymbol{\sigma} = \mathbf{C}_e : \boldsymbol{\varepsilon} \\ \mathbf{m} = \mathbf{A}_e : \boldsymbol{\chi} \end{cases} \quad \text{on} \;\; \Omega_e \, , \tag{6}$$

where $\mathbf{C}_e$ and $\mathbf{A}_e$ are, respectively, linear elasticity and couple stress elasticity tensors whose matrix expressions in (x, y, z) are given in Appendix A. We note that the couple stress elasticity coefficients expressed in (x, y, z), $(A_e)_{ijkl} = (C_e)_{ijkl} l^2$, are a function of l, which refers to the material length scale parameter. Commonly determined experimentally, the parameter l measures the couple stress effect [27][28] and leads to the size dependence of the couple stress model.

The actuators and sensors (Ω_p) are deformable continuum with properties of piezoelectricity. Therefore, the associated constitutive relations simultaneously account for the effects of piezoelectricity, couple stress elasticity and their coupling. Hence, we have

$$\begin{cases} \boldsymbol{\sigma} = \mathbf{C}_p : \boldsymbol{\varepsilon} - \mathbf{e} \cdot \mathbf{E} \\ \mathbf{D} = \mathbf{e} : \boldsymbol{\varepsilon} + \boldsymbol{\epsilon} \cdot \mathbf{E} \\ \mathbf{m} = \mathbf{A}_p : \boldsymbol{\chi} \end{cases} \quad \text{on} \;\; \Omega_p \, , \tag{7}$$

where $\mathbf{C}_p$ and $\mathbf{A}_p$ characterise the linear elasticity and couple stress elasticity for the piezoelectric patches. Regarding the piezoelectric properties, we use $\mathbf{e}$ to denote piezoelectricity tensor and $\boldsymbol{\epsilon}$ the permittivity tensor. Components of $\mathbf{e}$ and $\boldsymbol{\epsilon}$ expressed in (x, y, z) are given as follows:

$$[e_{ijk}]_{3\times 5} = \begin{bmatrix} 0 & 0 & 0 & e_{15} & 0 \\ 0 & 0 & e_{15} & 0 & 0 \\ e_{31} & e_{31} & 0 & 0 & 0 \end{bmatrix} , \tag{8}$$

and

$$[\epsilon_{ij}] = \begin{bmatrix} \epsilon_{11} & 0 & 0 \\ 0 & \epsilon_{11} & 0 \\ 0 & 0 & \epsilon_{33} \end{bmatrix} . \tag{9}$$

Equation of couple stress elasto-dynamics

By considering distinct material properties for Ω_e and Ω_p, we can write the kinetic energy K of the system as

$$K = \frac{1}{2}\int_{\Omega_e} \rho_e \dot{\mathbf{u}}^2 \mathrm{d}\Omega + \frac{1}{2}\int_{\Omega_p} \rho_p \dot{\mathbf{u}}^2 \mathrm{d}\Omega \,, \tag{10}$$

where ρ_e and ρ_p are densities of Ω_e and Ω_p, respectively. Considering both the kinetic energy [10] and the Gibbs free energy given in [1], we obtain the Gibbs-type variational principle

$$\delta\Pi_G = \delta G - \delta K \,. \tag{11}$$

By introducing (6,7) into (1), then the obtained Gibbs free energy (1) and kinetic energy (10) into (11), with the Gibbs-type variational principle which writes $\delta\Pi_G = 0$, we obtain the governing equation of couple stress elasto-dynamics

$$\begin{aligned}
&\int_{\Omega_e} \delta\boldsymbol{\varepsilon} : \mathbf{C}_e : \boldsymbol{\varepsilon}\mathrm{d}\Omega + \int_{\Omega_a} \delta\boldsymbol{\varepsilon} : \mathbf{C}_p : \boldsymbol{\varepsilon}\mathrm{d}\Omega + \int_{\Omega_s} \delta\boldsymbol{\varepsilon} : \mathbf{C}_p : \boldsymbol{\varepsilon}\mathrm{d}\Omega \\
&- \int_{\Omega_a} \delta\boldsymbol{\varepsilon} : \mathbf{e} \cdot \mathbf{E}_a \mathrm{d}\Omega - \int_{\Omega_s} \delta\boldsymbol{\varepsilon} : \mathbf{e} \cdot \mathbf{E}_s \mathrm{d}\Omega + \int_{\Omega_a} \delta\boldsymbol{\chi} : \mathbf{A}_p : \boldsymbol{\chi}\mathrm{d}\Omega \\
&+ \int_{\Omega_s} \delta\boldsymbol{\chi} : \mathbf{A}_p : \boldsymbol{\chi}\mathrm{d}\Omega + \int_{\Omega_e} \delta\boldsymbol{\chi} : \mathbf{A}_e : \boldsymbol{\chi}\mathrm{d}\Omega \\
&- \int_{\Omega_a} \delta\mathbf{E}_a \cdot (\mathbf{e} : \boldsymbol{\varepsilon} + \epsilon \cdot \mathbf{E}_a)\,\mathrm{d}\Omega - \int_{\Omega_s} \delta\mathbf{E}_s \cdot (\mathbf{e} : \boldsymbol{\varepsilon} + \boldsymbol{\epsilon} \cdot \mathbf{E}_s)\,\mathrm{d}\Omega \\
= &- \left(\int_{\Omega_e} \rho_e \ \ddot{\mathbf{u}} \cdot \delta\mathbf{u}\mathrm{d}\Omega + \int_{\Omega_p} \rho_p \ \ddot{\mathbf{u}} \cdot \delta\mathbf{u}\mathrm{d}\Omega \right) \,,
\end{aligned} \tag{12}$$

where the domain occupied by sensors Ω_s and actuators Ω_a are integrated separately, with $\Omega_p = \Omega_s \cup \Omega_a$. We note distinct electric fields $\mathbf{E}_s$ and $\mathbf{E}_a$ on the sensors and actuators. However, since they are made of the same material, we do not distinguish elastic behaviours $\mathbf{C}_p$, $\mathbf{A}_p$ and piezoelectric coefficients $\mathbf{e}$ between sensors and actuators.

3 FEM implementation using a $Q4$ Mindlin micro plate finite element

Finite element implementation of the modified couple stress elasto-dynamics requires at least nodal compatibility with C_1 continuity due to the presence of second-order derivatives of displacements. To meet this requirement, we adopt in this work a four-node quadrilateral plate element with non-conforming formulation, developed by Melosh and Zienkiewicz and Cheung (MZC) [26]. Although C_1 discontinuous on the inter-element boundary, this element preserves nodal C_1 continuity and therefore can be considered as a tolerable solution for high-order elasticity implementation.

3.1 Basic kinematics

Basic kinematics of the Mindlin plate is illustrated in Fig.(2). We consider a plate structure of thickness h subject to uniform force load q and in-plane couple load (pure moment) m_x and m_y, respectively around x and y axis. Displacement of the plate continuum is described by $u\,(x, y, z)$, $v\,(x, y, z)$ and

$w(x,y,z)$ which are components along x, y and z axis. Kinematics of the plate mid-plane involves both the displacement components $u(x,y)$, $v(x,y)$ and $w(x,y)$ and rotation components $\phi_x(x,y)$ and $\phi_y(x,y)$, and we focus on the anti-plane wave propagation which is predominant in the micro plate structures. Effects of membrane displacements $u(x,y)$ and $v(x,y)$ are ignored.

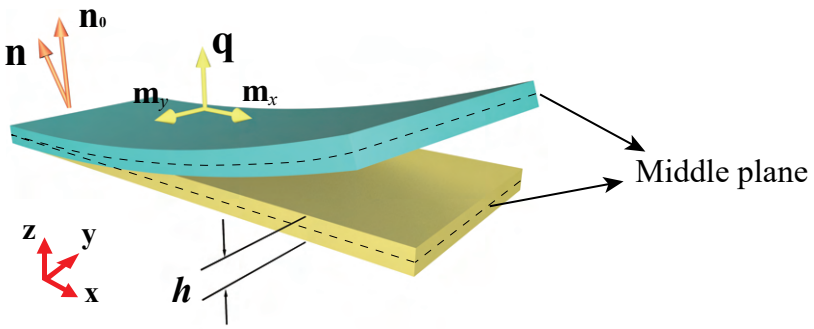

Figure 2: Mindlin plate kinematics: initial and deformed configurations.

Using the above parameters, we prescribe basic kinematic relations that respect the classical Mindlin plate assumptions [29] that we recall as follows: (1) Constant plate thickness during deformation. (2) *Plane-stress* assumption stipulating negligible normal stress through the plate thickness. (3) Linear variation of displacement across thickness. As a result, the plate cross section remains flat but not necessarily perpendicular to the mid-plane during deformation. In addition, we suppose negligible in-plane stretching in the context of vibroacoustic analysis, for which the effects of deflections and rotations dominate. Therefore, displacement components of the Mindlin plate can be written as

$$\begin{aligned} u(x,y,z) &= -z\phi_x(x,y), \\ v(x,y,z) &= -z\phi_y(x,y), \\ w(x,y,z) &= w_0(x,y), \end{aligned} \tag{13}$$

where ϕ_x and ϕ_y refer to rotations around x and y axis, respectively; w_0 is the displacement in z direction of the plate mid-plane. We then prescribe with respect to the above description nodal kinematic parameters that involve deflections, rotations and their derivatives to satisfy the compatibility with couple stress continuum. This leads to a vector of nine nodal degrees of freedom, which writes for the node i as

$$\{\mathbf{u}_i\}_{9\times 1} = \left[w \quad \phi_x \quad \phi_y \quad \frac{\partial w}{\partial x} \quad \frac{\partial \phi_x}{\partial x} \quad \frac{\partial \phi_y}{\partial x} \quad \frac{\partial w}{\partial y} \quad \frac{\partial \phi_x}{\partial y} \quad \frac{\partial \phi_y}{\partial y} \right]^T. \tag{14}$$

With the kinematics described by Eqs.(13,14), we are ready to derive strain components in accordance with both the classical theory of elasticity and the high order couple stress continuum.

Cauchy strain ε expression

Relations of classical elasticity are established using Cauchy strains based on first derivatives of Eq.(13). Components of Cauchy strain can be written as the product between a transformation matrix $[\mathbf{S}_\varepsilon]$ and a generalised strain $\{\hat{\boldsymbol{\varepsilon}}\}$, which gives

$$\{\boldsymbol{\varepsilon}\} = [\mathbf{S}_\varepsilon]\{\hat{\boldsymbol{\varepsilon}}\}, \tag{15}$$

where the transformation matrix $[\mathbf{S}_\varepsilon]$ writes

$$[\mathbf{S}_\varepsilon] = \begin{bmatrix} -z & & & & \\ & -z & & & \\ & & 1 & & \\ & & & 1 & \\ & & & & -z \end{bmatrix} , \tag{16}$$

and the generalised strain $\hat{\boldsymbol{\varepsilon}}$ involving both in-plane and out-of-plane components writes

$$\{\hat{\boldsymbol{\varepsilon}}\} = \begin{bmatrix} \frac{\partial \phi_x}{\partial x} \\ \frac{\partial \phi_y}{\partial y} \\ \frac{\partial w_0}{\partial y} - \phi_y \\ \frac{\partial w_0}{\partial x} - \phi_x \\ \frac{\partial \phi_x}{\partial y} + \frac{\partial \phi_y}{\partial x} \end{bmatrix} . \tag{17}$$

Here, generalised strain $\{\hat{\boldsymbol{\varepsilon}}\}$ derives from the displacement field using

$$\{\hat{\boldsymbol{\varepsilon}}\} = [\mathbf{B}_\varepsilon]\{\mathbf{u}\} , \tag{18}$$

with the strain-displacement matrix $[\mathbf{B}_\varepsilon]$ provided in Appendix B.

Symmetric curvature tensor $\boldsymbol{\chi}$ expression

Kinematics description based on couple stress continuum requires expression of symmetric curvature $\{\boldsymbol{\chi}\}$, whose components are second derivatives of the plate displacement (Eq.(13)). Similar to Cauchy strain (Eq.(15)), $\{\boldsymbol{\chi}\}$ can also be expressed as the product between a transformation matrix $[\mathbf{S}_\chi]$ and a generalised strain $\{\hat{\boldsymbol{\chi}}\}$, therefore

$$\{\boldsymbol{\chi}\} = [\mathbf{S}_\chi]\{\hat{\boldsymbol{\chi}}\} , \tag{19}$$

where the transformation matrix $\mathbf{S}_\chi$ writes

$$[\mathbf{S}_\chi] = \begin{bmatrix} \frac{1}{2} & & & & \\ & -\frac{1}{2} & & & \\ & & -\frac{z}{2} & & \\ & & & -\frac{z}{2} & \\ & & & & \frac{1}{2} \end{bmatrix} , \tag{20}$$

and the generalised curvature $\{\hat{\boldsymbol{\chi}}\}$ involving first and second in-plane and out-of-plane derivatives of the displacement field, writes

$$\{\hat{\boldsymbol{\chi}}\} = \begin{bmatrix} \frac{\partial^2 w_0}{\partial y \partial x} + \frac{\partial \phi_y}{\partial x} \\ \frac{\partial^2 w_0}{\partial x \partial y} + \frac{\partial \phi_x}{\partial y} \\ \frac{\partial^2 \phi_y}{\partial x^2} - \frac{\partial^2 \phi_x}{\partial y \partial x} \\ \frac{\partial^2 \phi_y}{\partial x \partial y} - \frac{\partial^2 \phi_x}{\partial y^2} \\ \left(\frac{\partial^2 w_0}{\partial y^2} + \frac{\partial \phi_y}{\partial y}\right) - \left(\frac{\partial^2 w_0}{\partial x^2} + \frac{\partial \phi_x}{\partial x}\right) \end{bmatrix} . \tag{21}$$

Generalised curvature $\{\hat{\boldsymbol{\chi}}\}$ derives from the displacement field using

$$\{\hat{\boldsymbol{\chi}}\} = [\mathbf{B}_\chi]\{\mathbf{u}\} , \tag{22}$$

with the curvature-displacement matrix $[\mathbf{B}_\chi]$ also provided in Appendix B.

3.2 Implementation of the interpolation functions

Finite element implementation of couple stress continuum requires interpolation of nodal parameters that satisfy at least C_1 continuity at the nodes since second derivatives of displacement are involved as shown in Eq.(21). However, strict C_1 continuous interpolation is difficult to achieve as it requires either important number of nodal parameters or complex element topology. Instead of strict C_1 element continuity, we implement here a non-conforming element based on MZC 4-node interpolation. Although discontinuous for displacement derivatives on the element boundary, this formulation preserves C_1 continuity at the nodes. Given the nodal parameters in Eq.(14), we compose the element displacement vector for the 4-node formulation as follows

$$\{\mathbf{u}^e\}_{36\times 1} = \begin{bmatrix}\mathbf{u}_1^T & \mathbf{u}_2^T & \mathbf{u}_3^T & \mathbf{u}_4^T\end{bmatrix}^T . \tag{23}$$

Therefore, we obtain the approximate displacement field by interpolating nodal displacements with the non-conforming Hermite cubic shape functions[17]

$$\begin{aligned} w &= \sum_{i=1}^{4} N_i w_i + N_{i\xi}\frac{\partial w_i}{\partial \xi} + N_{i\eta}\frac{\partial w_i}{\partial \eta} \\ \phi_x &= \sum_{i=1}^{4} N_i \phi_{xi} + N_{i\xi}\frac{\partial \phi_{xi}}{\partial \xi} + N_{i\eta}\frac{\partial \phi_{xi}}{\partial \eta} \\ \phi_y &= \sum_{i=1}^{4} N_i \phi_{yi} + N_{i\xi}\frac{\partial \phi_{yi}}{\partial \xi} + N_{i\eta}\frac{\partial \phi_{yi}}{\partial \eta} \ , \end{aligned} \tag{24}$$

in which the shape function expressions are

$$\begin{aligned} N_i &= \frac{1}{8}\left(1+\xi_i\xi\right)\left(1+\eta_i\eta\right)\left(2+\xi_i\xi+\eta_i\eta-\xi^2-\eta^2\right) \\ N_{i\xi} &= \frac{1}{8}a\xi_i\left(1+\xi_i\xi\right)^2\left(1+\eta_i\eta\right)\left(\xi_i\xi-1\right) \\ N_{i\eta} &= \frac{1}{8}b\eta_i\left(1+\xi_i\xi\right)\left(\eta_i\eta-1\right)\left(1+\eta_i\eta\right)^2 \ , \end{aligned} \tag{25}$$

and (ξ_i, η_i) with $i = 1, 2, 3, 4$, refers to positions of the i-th vertex in the reference coordinates. a and b refer to the half side length of the rectangular element along x and y directions, respectively.

4 Feedback control and its implementation

Similar to the way generalised strains derive from nodal displacements (Eqs.(18,22)), we express element actuator/sensor electric field as function of the respective nodal voltage V_a and V_s which are scalar parameters. Therefore, from Eq.(5) we have:

$$\begin{aligned} \{\mathbf{E}_a\} &= [\mathbf{B}_V]\{V_a\} \\ \{\mathbf{E}_s\} &= [\mathbf{B}_V]\{V_s\} \ , \end{aligned} \tag{26}$$

where

$$\{\mathbf{B}_V\} = \begin{bmatrix} 0 & 0 & \frac{1}{h_p} \end{bmatrix}^T \ , \tag{27}$$

with h_p the thickness of the actuator/sensor patches. With the account for Eqs.(18,22,27), we introduce Cauchy strain (Eq.(15)), symmetric curvature (Eq.(19)) and electric field $\mathbf{E}_{a/s}$ (Eq.(26)) into the problem governing equation (Eq.(12)). After separation of kinematics parameters $\{\mathbf{u}^e\}$ from the actuator/sensor voltages $\{V_{a/s}\}$, we obtain the governing equation for the coupled system of piezoelectric Mindlin micro plate, that we express in the following form:

$$\begin{bmatrix} \mathbf{m}_{11} & \mathbf{0} & \mathbf{0} \\ \mathbf{0} & 0 & 0 \\ \mathbf{0} & 0 & 0 \end{bmatrix} \begin{bmatrix} \ddot{\mathbf{u}}^e \\ \ddot{V}_a \\ \ddot{V}_s \end{bmatrix} + \begin{bmatrix} \mathbf{k}_{11} & \mathbf{k}_{12} & \mathbf{k}_{13} \\ \mathbf{k}_{21} & \mathbf{k}_{22} & 0 \\ \mathbf{k}_{31} & 0 & \mathbf{k}_{33} \end{bmatrix} \begin{bmatrix} \mathbf{u}^e \\ V_a \\ V_s \end{bmatrix} = \begin{bmatrix} \mathbf{0} \\ 0 \\ 0 \end{bmatrix} . \tag{28}$$

Complete expressions of the components $[\mathbf{k}_{ij}]$ and $[\mathbf{m}_{11}]$ are given in Appendix C. As shown in Eq.(28), the coupled system involves element kinematics parameters $\{\mathbf{u}^e\}$ and sensing/actuating voltages V_s and V_a. During the operation of the system, the sensing voltage V_s is generated on piezoelectric sensors due to vibration induced elastic deformation. Meanwhile, the induced V_s is fed back to the actuator after the current goes through an external controller on which a control algorithm is implemented. The control algorithm solves V_a as function of V_s and determines the vibroacoustic behaviour of the coupled piezoelectric micro system. In this work, the feedback control strategy is designed by considering the combination of direct proportional control [25], constant gain negative velocity control [25] and acceleration feedback control [5] strategies. V_a is solved as function of V_s and its derivatives, as

$$V_a = -g_a \frac{\partial^2 V_s}{\partial t^2} - g_b \frac{\partial V_s}{\partial t} - g_c V_s \, . \tag{29}$$

Voltage gain observed on V_a with respect to V_s is proportional to three parameters V_s, $\dot{V}_s$ and $\ddot{V}_s$, which correspond to the effects of displacement, velocity and acceleration, respectively. By adjusting g_a, g_b and g_c, we can prescribe dependence on these parameters based on their combinations. Adding feedback control to the coupled system, we substitute Eq.(29) into Eq.(28) and obtain the condensed system:

$$[\ \mathbf{m}^*]\{\ddot{\mathbf{u}}^e\} + [\ \mathbf{c}^*]\{\dot{\mathbf{u}}^e\} + [\ \mathbf{k}^*]\{\mathbf{u}^e\} = \{\mathbf{0}\} \, , \tag{30}$$

where

$$\begin{aligned} [\mathbf{m}^*] &= [\mathbf{m}_{11}] + g_a[\mathbf{k}_{12}][\mathbf{k}_{33}]^{-1}[\mathbf{k}_{31}] \\ [\ \mathbf{c}^*] &= g_b[\mathbf{k}_{12}][\mathbf{k}_{33}]^{-1}[\mathbf{k}_{31}] \\ [\ \mathbf{k}^*] &= [\mathbf{k}_{11}] + g_c[\mathbf{k}_{12}][\mathbf{k}_{33}]^{-1}[\mathbf{k}_{31}] - [\mathbf{k}_{13}][\mathbf{k}_{33}]^{-1}[\mathbf{k}_{31}] \, . \end{aligned}$$

The presence of first order derivatives in Eq.(29) yields equivalent effect of damping as seen in Eq.(30) which contributes to the control of vibrations. On the base plate outside the sensor/actuator binding area, Eq.(28) no longer applies. The model is undamped whose governing equation reads:

$$[\mathbf{m}]\{\ddot{\mathbf{u}}^e\} + [\mathbf{k}]\{\mathbf{u}^e\} = \{\mathbf{0}\} \, , \tag{31}$$

for which the component matrices are given in Appendix C. The complete model of the piezoelectric coupled system involves both Eq.(30) for the three-layer sensor-plate-actuator coupled structure, and Eq.(31) for the remaining area of the base plate which is subject of undamped vibration. Modal extraction based on Eqs.(30,31) is not a trivial task due to the asymmetric $[\mathbf{c}^*]$ matrix in the second-order dynamic equation Eq.(30). To overcome this difficulty, we adopt the state-space representation of Eq.(30) which leads to a first-order differential equation. Let $\{\mathbf{Z}\} = \left[(\dot{\mathbf{u}}^e)^T \ (\mathbf{u}^e)^T\right]^T$, we transform Eq.(30) to:

$$[\mathbf{B}]\{\dot{\mathbf{Z}}\} + [\mathbf{G}]\{\mathbf{Z}\} = \{\mathbf{0}\} \, , \tag{32}$$

where

$$[\mathbf{B}] = \begin{bmatrix} \mathbf{0} & \mathbf{m}^* \\ \mathbf{m}^* & \mathbf{c}^* \end{bmatrix}, \quad [\mathbf{G}] = \begin{bmatrix} -\mathbf{m}^* & \mathbf{0} \\ \mathbf{0} & \mathbf{k}^* \end{bmatrix}.$$

By considering the displacement field in time domain under the form

$$\{\mathbf{Z}(\mathbf{r}, t)\} = \{\mathbf{Z}_0(\mathbf{r}) e^{i\omega t}\}, \tag{33}$$

we transform Eq.(32) to frequency domain, which leads to:

$$([\mathbf{G}] + i\omega[\mathbf{B}])\{\mathbf{Z}_0\} = \{\mathbf{0}\}, \tag{34}$$

in which

$$\{\mathbf{Z}_0\} = \begin{bmatrix} (\dot{\mathbf{u}}_0^e)^T & (\mathbf{u}_0^e)^T \end{bmatrix}^T. \tag{35}$$

Since the unknown vector $\{\mathbf{Z}_0\}$ contains both $\{\dot{\mathbf{u}}_0^e\}$ and $\{\mathbf{u}_0^e\}$, the boundary conditions of the original modal problem requires adaptation before implementation. Details will be given in Section 5.

5 Implementation of the band gap unit cell boundary value problem

Band gap analysis is performed by solving a unit cell boundary value problem that we depict in Fig.(3). The unit cell finite element model is composed of three-layer Mindlin micro plate elements for the area of the base plate with piezoelectric patches, and single-layer Mindlin micro plate elements for the rest of the base plate. Material properties of the piezoelectric patches and of the base plate are integrated through their thicknesses and expressed with respect to the plate mid-surface. Hence, the mid-surface of the heterogeneous unit cell is depicted in Fig.(3). The unit cell dimension is described

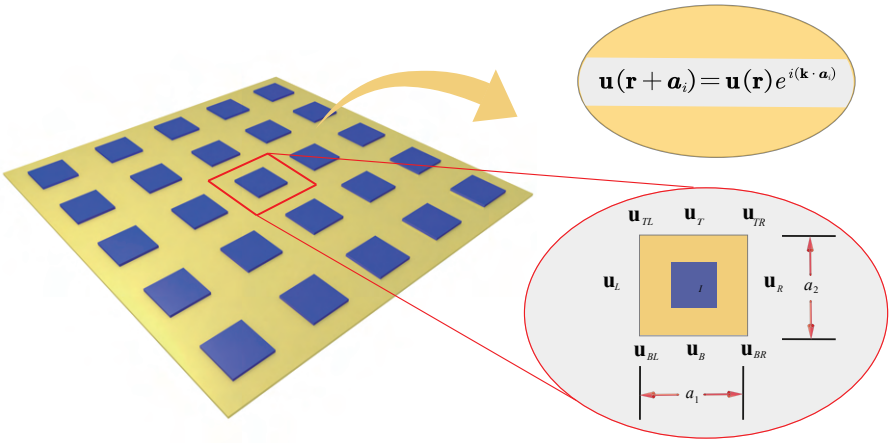

Figure 3: Periodic piezoelectric micro plate system and its unit cell. Since material properties of Ω_p and Ω_e are pre-integrated through the thickness and expressed on the mid-surface, the figure depicts the structural and material heterogeneities projected to the mid-surface of the unit cell.

by its edge lengths along x and y axis, denoted by a_1 and a_2, respectively. To clearly describe the periodic boundary conditions on the unit cell, we use $\{\mathbf{u}_L\}$, $\{\mathbf{u}_R\}$, $\{\mathbf{u}_T\}$ and $\{\mathbf{u}_B\}$ to denote nodal displacements on the left (L), right (R), top (T) and bottom (B) edges of the unit cell except at the corner nodes. Then, we use $\{\mathbf{u}_{TL}\}$, $\{\mathbf{u}_{TR}\}$, $\{\mathbf{u}_{BL}\}$ and $\{\mathbf{u}_{BR}\}$ to denote displacements of the top-left

(TL), top-right (TR), bottom-left (BL) and bottom-right (BR) corner nodes. In the end, we use $\{\mathbf{u}_I\}$ to denote displacements of internal nodes of the domain. Using the above notations, we implement the Bloch boundary conditions by considering $\lambda_1 = e^{i\boldsymbol{k}\cdot\boldsymbol{a_1}}$ and $\lambda_2 = e^{i\boldsymbol{k}\cdot\boldsymbol{a_2}}$, in addition to the periodic conditions that relate $\{\mathbf{u}_R\}$ to $\{\mathbf{u}_L\}$, $\{\mathbf{u}_T\}$ to $\{\mathbf{u}_B\}$, then at the corner nodes with $\{\mathbf{u}_{BR}\}$, $\{\mathbf{u}_{TR}\}$ and $\{\mathbf{u}_{TL}\}$ with respect to $\{\mathbf{u}_{BL}\}$. The displacement vector for the unit cell can be expressed in the following form

$$\{\mathbf{u}\} = \begin{bmatrix} \mathbf{u}_I \\ \mathbf{u}_L \\ \mathbf{u}_R \\ \mathbf{u}_B \\ \mathbf{u}_T \\ \mathbf{u}_{BL} \\ \mathbf{u}_{BR} \\ \mathbf{u}_{TR} \\ \mathbf{u}_{TL} \end{bmatrix} = \begin{bmatrix} \mathbf{I} & \mathbf{0} & \mathbf{0} & \mathbf{0} \\ \mathbf{0} & \mathbf{I} & \mathbf{0} & \mathbf{0} \\ \mathbf{0} & \lambda_1\mathbf{I} & \mathbf{0} & \mathbf{0} \\ \mathbf{0} & \mathbf{0} & \mathbf{I} & \mathbf{0} \\ \mathbf{0} & \mathbf{0} & \lambda_2\mathbf{I} & \mathbf{0} \\ \mathbf{0} & \mathbf{0} & \mathbf{0} & \mathbf{I} \\ \mathbf{0} & \mathbf{0} & \mathbf{0} & \lambda_1\mathbf{I} \\ \mathbf{0} & \mathbf{0} & \mathbf{0} & \lambda_1\lambda_2\mathbf{I} \\ \mathbf{0} & \mathbf{0} & \mathbf{0} & \lambda_2\mathbf{I} \end{bmatrix} \begin{bmatrix} \mathbf{u}_I \\ \mathbf{u}_L \\ \mathbf{u}_B \\ \mathbf{u}_{BL} \end{bmatrix} = [\mathbf{P}]\{\widetilde{\mathbf{u}}\} \ . \tag{36}$$

Similarly, the unknown vector $\{\mathbf{Z_0}\}$ in Eq.(35) for the state-space resolution with the account for periodic boundary conditions can be written as

$$\{\mathbf{Z}_0\} = \begin{bmatrix} \mathbf{P}^T & \mathbf{0} \\ \mathbf{0} & \mathbf{P}^T \end{bmatrix} \{\tilde{\mathbf{Z}}_0\} \ , \tag{37}$$

with $\{\tilde{\mathbf{Z}}_0\} = \begin{bmatrix} (\dot{\widetilde{\mathbf{u}}}_0)^T & (\widetilde{\mathbf{u}}_0)^T \end{bmatrix}^T$, which means

$$\{\tilde{\mathbf{Z}}_0\} = \begin{bmatrix} (\dot{\mathbf{u}}_0^I)^T & (\dot{\mathbf{u}}_0^L)^T & (\dot{\mathbf{u}}_0^B)^T & (\dot{\mathbf{u}}_0^{BL})^T & (\mathbf{u}_0^I)^T & (\mathbf{u}_0^L)^T & (\mathbf{u}_0^B)^T & (\mathbf{u}_0^{BL})^T \end{bmatrix}^T \ . \tag{38}$$

Introducing Eq.(37) into the original unit cell modal problem Eq.(34), we obtain its state-space representation with periodic boundary conditions:

$$\begin{bmatrix} \mathbf{P}^T & \mathbf{0} \\ \mathbf{0} & \mathbf{P}^T \end{bmatrix} ([\mathbf{G}] + i\omega[\mathbf{B}]) \begin{bmatrix} \mathbf{P} & \mathbf{0} \\ \mathbf{0} & \mathbf{P} \end{bmatrix} \{\tilde{\mathbf{Z}}_0\} = 0 \ . \tag{39}$$

Eq.(39) can be noted as:

$$\left([\bar{\mathbf{G}}] + i\omega[\bar{\mathbf{B}}]\right) \{\tilde{\mathbf{Z}}_0\} = \{\mathbf{0}\} \ , \tag{40}$$

where

$$[\bar{\mathbf{G}}] = [\bar{\mathbf{P}}]^T[\mathbf{G}][\bar{\mathbf{P}}], \quad [\bar{\mathbf{B}}] = [\bar{\mathbf{P}}]^T[\mathbf{B}][\bar{\mathbf{P}}], \quad \bar{\mathbf{P}} = \begin{bmatrix} \mathbf{P} & \mathbf{0} \\ \mathbf{0} & \mathbf{P} \end{bmatrix} \ . \tag{41}$$

The obtained Eq.(40) refers to the final form of the unit cell boundary value problem for modal analysis.

6 Numerical results

In this section, we study vibration behaviours of a piezoelectric micro plate system using the feedback control strategy proposed in in Section 4. The first example, in Section 6.1, validates the importance of size dependence in band gap properties for the micro plate coupled system. We subsequently propose a structure configuration that leads to significant size effect. Then, based on this configuration, we will perform band gap and frequency response analysis to examine the influence of multi-parameter control strategies. Both the effects of single-parameter control and multi-parameter control will be discussed

in Section 6.2 and Section 6.3, respectively.

6.1 Size dependence of band gap behaviours: microstructure effects

In this section, we study the significance of size effects in band gap behaviours for the piezoelectric micro plate coupled system and demonstrate the relevance of the modified couple stress model treating size effects. We prescribe two micro plate configurations of distinct length scales and investigate their band gap properties using both the couple stress and classical theories of elasticity. The two problems are distinct in size: one very small and the other on the macroscopic scale. We demonstrate through band gap calculations, that the couple stress and classical theory solutions agree on the macroscopic problem but diverge on the micro plate problem for which size effects emerge. Concerning the mechanism of vibration attenuation, the proposed three-parameter feedback control is tested using mass, damping and stiffness based control, configured respectively constant gain coefficients g_a, g_b and g_c, as indicated in Eq.(29).

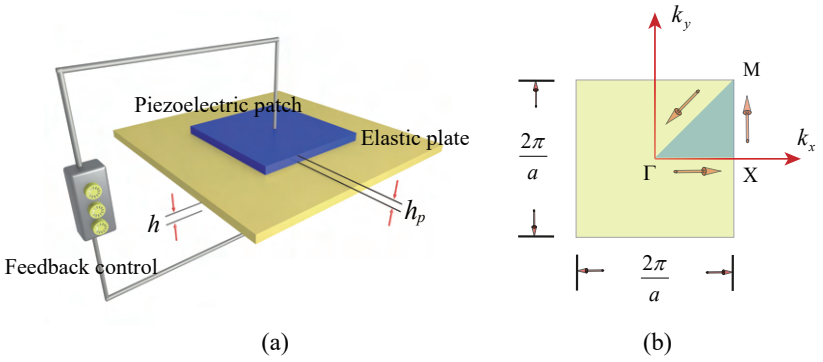

Figure 4: (a) Unite cell configuration (b) Irreducible first Brillouin zone

The test scenario is based on the piezoelectric micro plate system as shown in Fig.(4). The structure incorporates periodically distributed sensor and actuator patches whose unit cell geometry is given in Fig.(4a). For the micro scale model, the base plate thickness $h = 20$ μm. The unit cell is square in shape with edge length $a = 50 \times h$. The piezoelectric patches, both the sensors and actuators, are also square in shape with edge length $b = 0.8 \times a$. As a comparison, the macro scale model is significantly larger in size with $h = 120$ μm, the other geometry parameters are defined with respect to h like the micro scale model with the same proportion factors. For the two cases, we prescribe piezoelectric patch thickness $h_p = 3h$. Material composition of the unit cell can be distinguished between the base plate material (epoxy) and the piezoelectric plate material ($BiTiO_3$), whose properties are given in Tab. 1. The unit cell is discretised with the four-node quadrilateral element described in Section 3.2 using the same mesh for both the macro and micro scale cases.

Table 1: Unit cell material properties

	C_{11} (GPa)	C_{12} (GPa)	C_{44} (GPa)	e_{15} (C/m^2)	e_{31} (C/m^2)	ϵ_{11} (10^{-9}C^2/(N $\cdot$ m^2))	ϵ_{33} (10^{-9}C^2/(N $\cdot$ m^2))	l (μm)	ρ (g/cm^3)
Base plate	4.9	2.4	1.24	0	0	0	0	16.93	1.18
Piezoelectric plate	166	77	43	11.6	−4.4	11.2	12.6	7	5.8

Size dependence in band gap behaviours are examined with the activation of vibration control: the three feedback control strategies are prescribed independently by considering the following configurations: mass control with $g_b = g_c = 0, g_a = 2 \times 10^{-12}$, damping control with $g_a = g_c = 0, g_b = 1.5 \times 10^{-5}$

and stiffness control with $g_a = g_b = 0, g_c = 300$. A particular case of free vibration without vibration control ($g_a = g_b = g_c = 0$) is also investigated.

Calculation of band gap diagrams requires considering wave vectors on the boundary of the irreducible first Brillouin zone, which in the case of 2D symmetric domains, is presented in the form of a triangle as depicted in Fig.(4b). Modal analysis required for band gap calculations can be reduced to the boundary of the triangle by following the path $\Gamma-\mathrm{X}-\mathrm{M}-\Gamma$. In the present case, this leads to modal resolutions on 58 equidistant, discrete points along the path $\Gamma-\mathrm{X}-\mathrm{M}-\Gamma$. Specifically, we implement Floquet-periodic boundary conditions by considering the wave vector $\mathbf{k}_i = (k_x, k_y)$ $(i = 1, 2, \ldots, 58)$ which takes distinct forms on each section along the path $\Gamma-\mathrm{X}-\mathrm{M}-\Gamma$, in particular: from Γ to X, $k_x = \frac{2\pi}{a}k$, $k_y = 0$, $k \in [0, 1]$, from X to M, $k_x = \frac{2\pi}{a}$, $k_y = \frac{2\pi}{a}(k-1)$, $k \in [1, 2]$, from M to Γ, $k_x = \frac{2\pi}{a}(3-k)$, $k_y = \frac{2\pi}{a}(3-k)$, $k \in [2, 3]$.

The result band diagrams are presented in Fig.(5) for the two tested geometry settings which have been studied based on four configurations of control strategy, respectively. In total, eight problems have been examined using both couple stress (red curves) and classical (blue curves) elasto-dynamics. With Fig.(5(a-d)), we report band diagrams obtained from the micro scale problem for which the base plate thickness $h = 20$ μm. As a comparison, we report with Fig.(5(e-h)) band diagrams from the macro scale problem with $h = 120$ μm. Both micro and macro scale problems have been tested on four configurations of vibration control, consisting of: non feedback control (a,e); mass based control (b,f); damping based control (c,g) and stiffness based control (d,h). It is not difficult to observe that the couple stress and the classical elasto-dynamic models agreed with each other on the macro scale model but led to significantly different band diagrams on the micro scale model. The disagreement is particularly important in the high frequency range and reflects significant microstructure effects that emerged due to the small enough problem size of the micro scale problem setting. This observation confirms the problem size dependence of band gap behaviours for the tested piezoelectric micro plate systems. We also confirm that size dependence can be captured by the couples stress model but not by the classical elasticity model. For the macro scale problem, on the contrary, since size effect is negligible, we observed good agreement between the couple stress and the classical models according to (e-h). Based on all the tested cases, it becomes obvious that the emergence of microstructure effect only depends on the problem size and is irrelevant to the choice of the vibration control strategy. In conclusion, size effect is important to take into account in the design of piezoelectric micro plate systems. The implemented couple stress elasto-dynamic model provides a practical way to deal with size effects of such problems. In the following numerical examples, since vibration control with size effects will be explored, the unit cell configuration based on $h = 20$ μm will be adopted as the significance of size effects is confirmed.

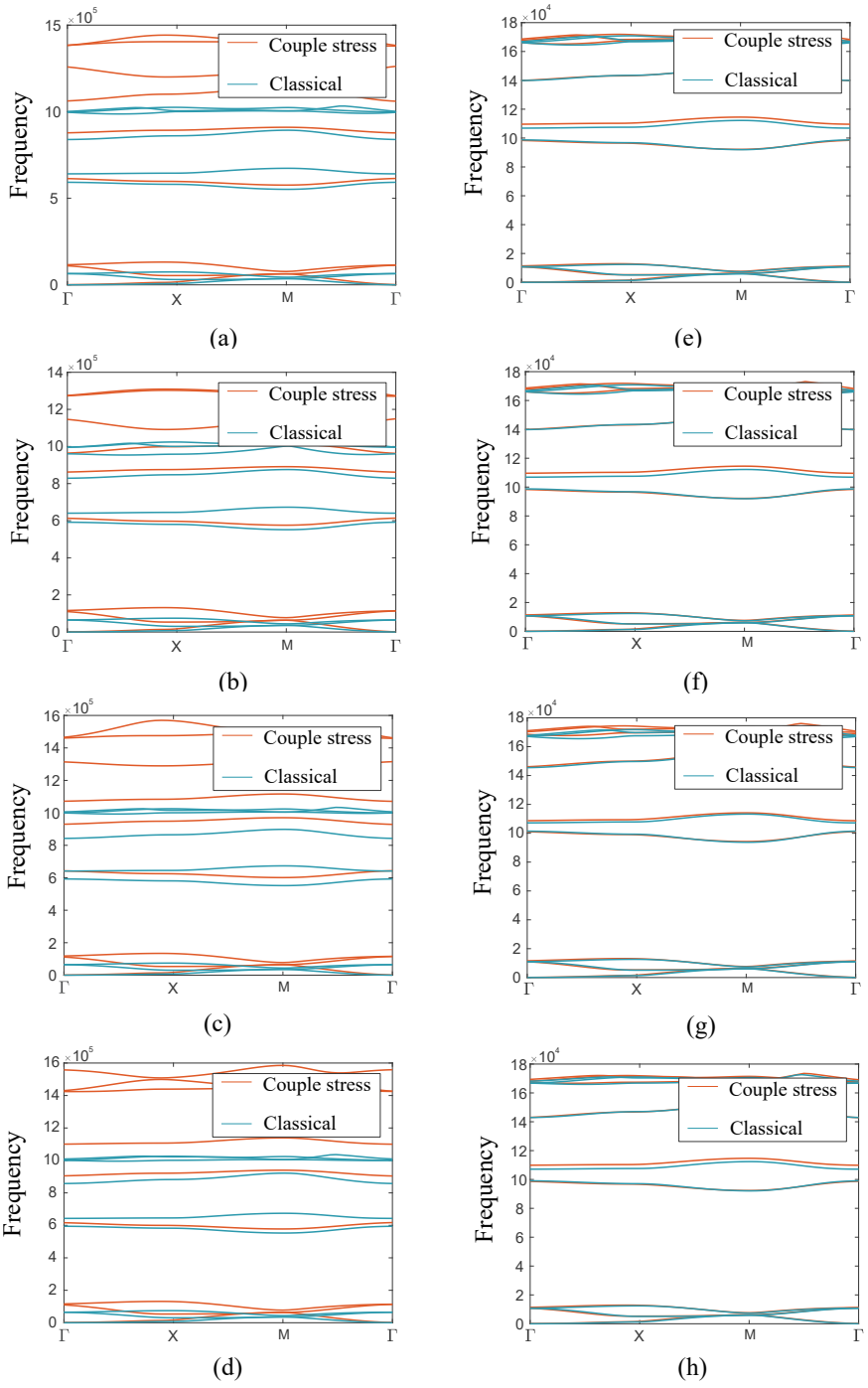

Figure 5: Band gap diagrams based on couple stress (red curves) and classical (blue curves) theories of elasto-dynamics: influence of problem sizes and control parameters. Cases (a-d) are based on the micro scale unit cell with $h = 20$ μm. Cases (e-h) are based on the macro scale unit cell with $h = 120$ μm. Four control strategies are tested using respectively: non feedback control (a,e) with $g_a = g_b = g_c = 0$; mass based control (b,f) with $g_a = 2 \times 10^{-12}$, $g_b = g_c = 0$; damping based control (c,g) with $g_b = 1.5 \times 10^{-5}$, $g_a = g_c = 0$; then, stiffness based control (d,h) with $g_c = 300$, $g_a = g_b = 0$.

6.2 Band gap tuning based on single-parameter control

The piezoelectric micro plate system incorporates a feedback control strategy that has been presented in Section 4. The control mechanism can be configured by three parameters g_a, g_b and g_c, which refer to the voltage gains within the sensor-to-actuator loop with respect to mass, damping and stiffness. In this section, we focus on the individual effect of the three control parameters and examine their respective influence on the vibration response of the coupled system. In particular, we prescribe three groups of band gap analysis, each group with g_a, g_b and g_c evolving on an interval of values. In addition, to understand how band gap results can be used to advise real structure design, we perform dynamic response analysis in frequency domain based on a representative structure composed of periodic unit cells and compare the result with band gap predictions. The computational protocol that we present in this section can be used to assist the parametrisation of the feedback controller, permitting tuning of band gap behaviours of the micro plate coupled system. We adopt the micro scale unit cell with the base plate thickness $h = 20$ μm. This configuration demonstrates significant size dependence of band gap behaviours according to Section 6.1. Therefore, application of the couple stress elasticity is justified.

Other geometry parameters of the unit cell is identical to the micro scale problem studied in Section 6.1, with $a = 1$ mm, $b = 0.8$ mm and $h_p = 3h$. Similarly, material composition of the unit cell is found in Tab. 1 of Section 6.1. We consider epoxy and $BiTiO_3$ for the base plate and sensor/actuator materials, respectively.

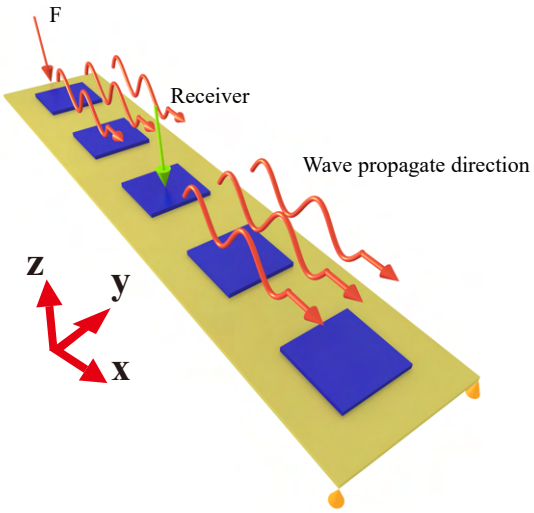

Figure 6: A five-cell system of coupled piezoelectric micro plate used for dynamic response analysis in frequency domain: orange pins indicate fixed DOFs; red arrow indicates input excitation; green arrow refers to the position of output wave measurement.

Band gap calculations are performed based on the periodic unit cell by considering the procedure presented in Section 6.1. To examine the effectiveness of the band gap results, we further conduct dynamic response analysis in frequency domain by prescribing a representative example of piezoelectric micro plate system composed of five unit cells periodically arranged along x direction, as shown in Fig.(6). Boundary conditions on the five-cell system are as follows: we fix all degrees of freedoms on the points $(x, y) = (5a, a)$ and $(x, y) = (5a, 0)$, and we prescribe $\mathrm{F_z} = \mathrm{F}e^{i\omega t}$ on the point $(x, y) = (0, a/2)$. The input wave signal then propagates along the micro plate structure and the steady-state dynamic response is collected on the point $(x, y) = (5a/2, a/2)$. The output dynamic response is then analysed with respect to the input excitation, allowing us to compare with the band gap results.

Dynamic response in frequency domain is obtained by using frequency response function (FRF) that

calculates steady-state dynamic response with regard to a sinusoidal input excitation. Let us consider a standard multi degree of freedom system with its state-space representation which writes

$$\mathbf{B}\dot{\mathbf{Z}} + \mathbf{G}\mathbf{Z} = \mathbf{F} \ . \tag{42}$$

Using Laplace transform, the corresponding transfer function denoted by $\mathbf{H}$ is written as

$$\mathbf{H} = \sum_{r=1}^{n} \frac{\boldsymbol{\phi}_r \boldsymbol{\phi}_r^T}{g_r + i\omega b_r} \ , \tag{43}$$

in which b_r, g_r are the r-th element on the diagonal of the matrices $\mathbf{B}$ and $\mathbf{G}$, respectively. $\boldsymbol{\phi}_r$ is the eigenvector associated with the r-th degree of freedom. Components of the transfer matrix, H_{ij}, can be physically interpreted as the dynamic response measured on point i with respect to an input excitation prescribed on point j.

Influence of g_a: mass based control

Effect of the control parameter g_a on the coupled micro plate system is studied. According to Eq.(29), g_a refers to the sensor-to-actuator voltage gain with respect to mass. Fig.(7a) focuses on the first four band gaps of the system and particularly the effect of g_a on the band gap frequency ranges. Therefore, as g_a is set to increase on the interval $[1 \times 10^{-12},\ 2.9 \times 10^{-12}]$, frequency ranges of the first

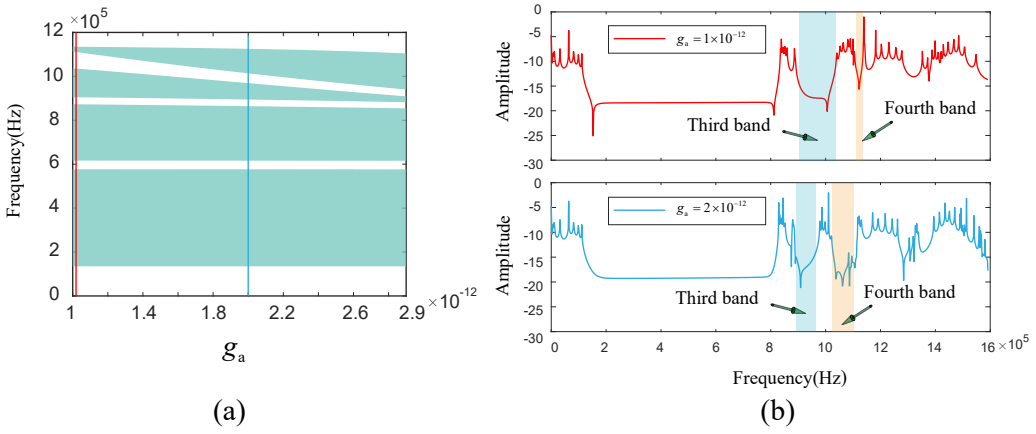

Figure 7: Effect of g_a on vibration control. (a) Evolution of the first four band gap frequency ranges with respect to g_a. (b) Dynamic response in frequency domain by considering two cases with $g_a = 1.0 \times 10^{-12}$ and $g_a = 2.0 \times 10^{-12}$. Positions of the third and the fourth band gaps calculated in (a) for the two cases, are highlighted on (b) to provide comparison.

and second band gaps remain almost constant, however, the third band gap is observed to decrease significantly and tends to vanish while g_a approaches the upper bound at 2.9×10^{-12}. Oppositely, a fourth band gap initiates at $g_a = 1.0 \times 10^{-12}$ and broadens with the increase of g_a. We report in Tab. 2 the frequency ranges of the third and fourth band gaps extracted from two cases based on g_a with $g_a = 1.0 \times 10^{-12}$ and $g_a = 2.0 \times 10^{-12}$, respectively. Results from Tab. 2 will be used in the following for comparison with dynamic response simulations in frequency domain.

Dynamic response analysis is performed based on a representative system of piezoelectric micro plate as depicted by Fig.(6). Amplitude of the dynamic response as function of the excitation frequency is reported in Fig.(7b). Here, for the dynamic response calculation, we consider the same cases as listed in Tab. 2, with $g_a = 1.0 \times 10^{-12}$ and $g_a = 2.0 \times 10^{-12}$. The results are presented using red and blue

Table 2: Third and fourth band gaps frequency range: effect of g_a

g_a setting	Third band gap (kHz)	Fourth band gap (kHz)
1.0×10^{-12}	$[905.01, 1036.60]$	$[1112.75, 1134.87]$
2.0×10^{-12}	$[891.31,\ 962.75]$	$[1011.36, 1091.49]$

curves, respectively. To facilitate comparison, we highlight in Fig.(7b) the third and fourth frequency ranges (Tab. 2) predicted by the unit cell model for the corresponding g_a settings. Therefore, we observed good agreement between the band gap and dynamic response models: firstly, the band gap frequency ranges predicted by the unit cell model are confirmed by the dynamic response simulation. Then, the broadened fourth band gap and the reduced third band gap predicted by the unit cell model, are also observed on the dynamic response curves. In summary, the control parameter g_a alone has negligible effect on the range of the first and second band gaps. It does affect band gaps of higher frequencies, that is to say, a greater g_a tends to reduce the third band gap but broadens the fourth band gap. Note however that the effect of g_a is presented in bounded ranges as shown in Tab. 2. With g_a beyond the presented ranges, the model may become unstable showing oscillating band gap results. Therefore, the effects of the control parameters are valid only within the respective validity ranges. This notice holds for the following examples.

Influence of g_b: damping based control

We now focus on the control parameter g_b and investigate its effect on the band gap of the coupled micro plate system. g_b governs the sensor-to-actuator voltage gain with respect to damping. We present in Fig.(8a) the first four band gaps of the system and their evolution with g_b. Here, similar to g_a, the effect of g_b is negligible on the first two band gaps and shows significance only on band gaps of higher frequencies. Therefore, with the increase of g_b on the interval $[0,\ 1.5 \times 10^{-5}]$, we observed broadened frequency range of the third and fourth band gaps.

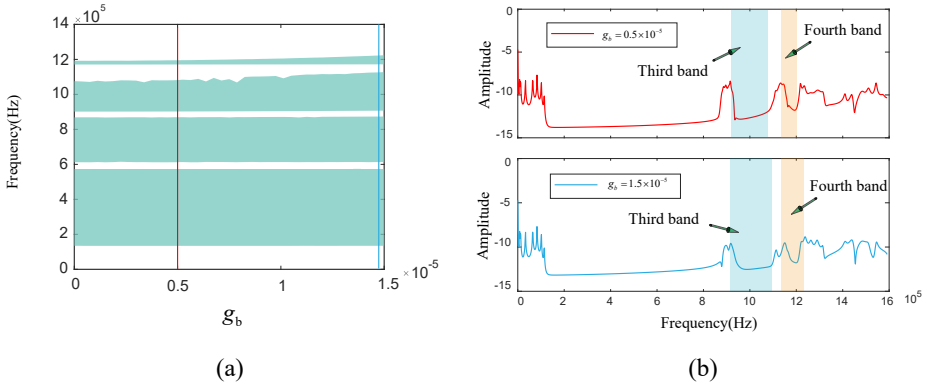

Figure 8: Effect of g_b on vibration control. (a) Evolution of the first four band gap frequency ranges with respect to g_b. (b) Dynamic response in frequency domain by considering two cases with $g_b = 0.5 \times 10^{-5}$ and $g_b = 1.5 \times 10^{-5}$. Positions of the third and the fourth band gaps calculated in (a) for the two cases, are highlighted on (b) to provide comparison.

To compare band gap predictions with dynamic response simulations, we report in Tab. 3 the frequency range of the third and fourth band gaps for two cases using $g_b = 0.5 \times 10^{-5}$ and $g_b = 1.5 \times 10^{-5}$, respectively.

Dynamic response analysis in frequency domain is performed by considering two cases of g_b with $g_b = 0.5 \times 10^{-5}$ and $g_b = 1.5 \times 10^{-5}$, whose response amplitude *vs.* excitation frequency is reported in

Table 3: Third and fourth band gaps frequency range: effect of g_b

g_b setting	Third band gap (kHz)	Fourth band gap (kHz)
0.5×10^{-5}	[910.61, 1066.37]	[1136.82, 1203.81]
1.5×10^{-5}	[915.63, 1094.14]	[1137.53, 1232.69]

Fig.(8b) using red and blue curves, respectively. The two dynamic response simulations are confronted to the band gap predictions that we have reported in Tab. 3. Also, to present a direct comparison between the two models, we highlight in Fig.(8b) the frequency range prediction of the third and the fourth band gaps obtained using the unit cell band gap calculation. Thus, good agreement can be observed between the band gap and dynamic response models. All the predicted band gaps can be localised on the dynamic response curves. From $g_b = 0.5 \times 10^{-5}$ to $g_b = 1.5 \times 10^{-5}$, we observed slightly broadened frequency ranges on both the third and the fourth band gaps, which is in accordance with the band gap prediction depicted in Fig.(8a). Similar to g_a, the effect of g_b on the system does not present significance on the first two band gaps, although it slightly affects the band gap ranges of higher frequencies, for instance, the third and the fourth band gap according to our test case.

Influence of g_c: stiffness based control

Finally, we move to investigate the influence of g_c on the bad gap of the coupled micro plate system. We remind that g_c refers to the sensor-to-actuator voltage gain with respect to stiffness according to Eq.(29). Again, similar to the two previous cases based on g_a and g_b, we observed negligible effect of g_c on the first two band gaps, but only on band gap ranges of higher frequencies. Hence, with increasing g_c on the interval $[0,\ 3.0 \times 10^2]$, we observed broadened frequency ranges for both the third and the fourth band gaps.

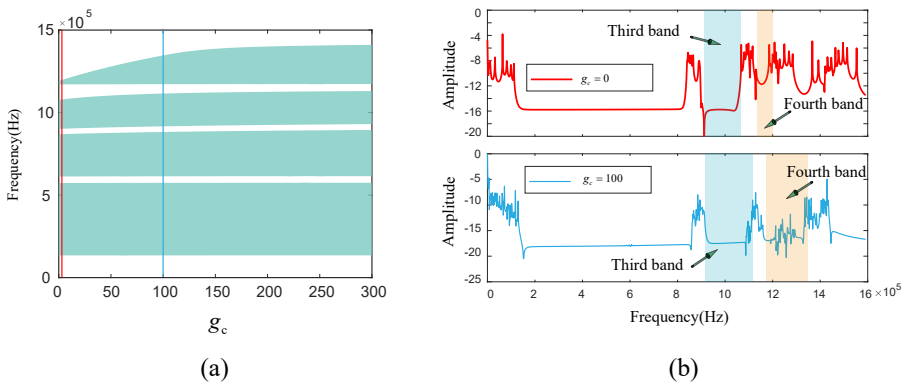

Figure 9: Effect of g_c on vibration control. (a) Evolution of the first four band gap frequency ranges with respect to g_c. (b) Dynamic response in frequency domain by considering two cases with $g_c = 0$ and $g_c = 1.0 \times 10^2$. Positions of the third and the fourth band gaps calculated in (a) for the two cases, are highlighted on (b) to provide comparison.

Based on the unit cell band gap calculation, frequency ranges of the third and fourth band gaps are extracted for $g_c = 0$ and $g_c = 1.0 \times 10^2$, whose results are presented in Tab. 4 and will be compared with dynamic response simulations.

We consider the two cases listed in Tab. 4 for the dynamic response analysis whose result depicts the response amplitude as function of the excitation frequencies in Fig.(9b). The two cases with $g_c = 0$ and $g_c = 1.0 \times 10^2$ are represented using red and blue curves, respectively. Similar to the two previous cases of g_a and g_b, we highlight in Fig.(9b) the frequency ranges of the third and the fourth band

Table 4: Third and fourth band gaps frequency range: effect of g_c

g_c setting	Third band gap (kHz)	Fourth band gap (kHz)
0	[909.92, 1060.12]	[1136.70, 1200.28]
1.0×10^2	[916.58, 1115.42]	[1172.20, 1346.64]

gaps predicted by the unit cell band gap calculation. This offers direct comparison with the dynamic response simulation and leads us to the following observation: firstly, all the predicted band gaps can be localised on the frequency response curves. Then, broadened frequency ranges are obtained on both the third and the fourth band gaps by comparing the $g_c = 1.0 \times 10^2$ case to the $g_c = 0$ case. This observation is conform to the band gap predictions in Fig.(9a). We observe again, however, that the effect of g_c on the first two band gaps is limited, it mainly affects the band gap ranges of middle to higher frequencies.

In summary, the control parameters g_a, g_b and g_c allow adjusting significantly higher frequency band gaps for the tested coupled micro plate system. In particular, mass based control (g_a) can be useful in controlling higher frequency vibrations since it allows lowering the lower bound of high-order band baps. In addition, damping (g_b) and stiffness (g_c) based control can both be applied to improve the range of medium and higher band gaps. Since the feedback control parameters affect notably the range of higher frequency band gaps, we will focus on higher order band gaps as an example to present the effect of multi-parameter control strategies in Section 6.3.

6.3 Tuning of higher frequency band gaps using multi-parameter control

Based on the coupled micro plate system studied in Section 6.1 and Section 6.2, we now consider multi-parameter control strategies involving combined effects of g_a, g_b and g_c on the tuning of vibration behaviours. Since these parameters demonstrate significant effect in adjusting higher order band gaps, we focus on the fourth band gap and investigate the effects of multi-parameter control based on combined effects of mass and damping (MD) control, mass and stiffness (MS) control, and, daming and stiffness (DS) control. Inspired by the methodologies presented in Section 6.2, we perform both unit cell band gap analysis and dynamic response calculations by considering a representative micro plate system consisted of five unit cells. Geometry and material definition of the unit cell and of the representative micro plate system is identical to the description given in Section 6.2.

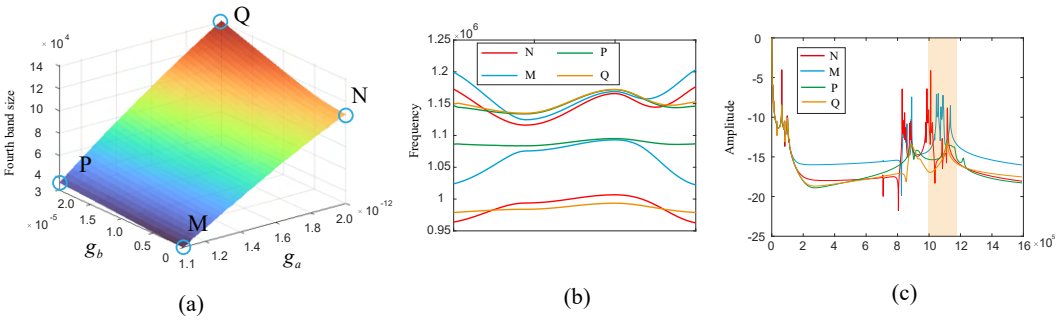

Figure 10: Effect of MD control: (a) Evolution of the fourth band gap size with respect to the combined effect of g_a and g_b simultaneously. (b) The fourth band gap diagrams considering cases N, M, P, Q. (c) Dynamic response in frequency domain based on a five unit cell couple micro plate system considering the cases N, M, P, Q.

We are first interested in the case of MD control strategy. Let $g_c = 0$, and g_a, g_b be the evolving

parameters. We calculate the range of the fourth band gap based on the periodic unit cell by considering g_a and g_b evolving on the intervals $[1.1 \times 10^{-12},\ 2.0 \times 10^{-12}]$ and $[0,\ 2.0 \times 10^{-5}]$, respectively. The result is reported in Fig.(10a), where the size of the fourth band gap is plotted as function of g_a and g_b combinations. Four cases, denoted by N, M, P, Q based on the combination of g_a and g_b are highlighted and the corresponding band diagrams depicting the fourth band gap ranges are provided in Fig.(10b). We note that the band gap size increases monotonically with respect to g_a and g_b on the tested intervals and the largest band gap is observed at point Q, with $g_a = 2.0 \times 10^{-12}$ and $g_b = 2.0 \times 10^{-5}$. Dynamic response analysis is performed on the five unit cell couple micro plate system using the same methodology as presented in Section 6.2. Response in frequency domain based on the four cases N, M, P, Q is reported in Fig.(10c) where the frequency range covered by the lowest and highest bounds for the four cases combined, predicted by the band gap unit cell calculation, is highlighted. From the frequency response curves in Fig.(10c), we can identify the fourth band gap for all the cases, which is covered by the highlighted band gap prediction.

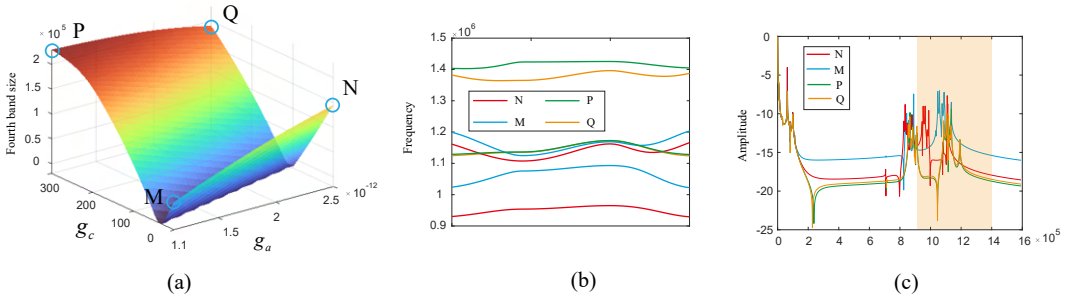

Figure 11: Effect of MS control: (a) Evolution of the fourth band gap size with respect to the combined effect of g_a and g_c simultaneously. (b) The fourth band gap diagrams considering cases N, M, P, Q. (c) Dynamic response in frequency domain based on a five unit cell couple micro plate system considering the cases N, M, P, Q.

We then focus on the case of MS control strategy for which $g_b = 0$ and g_a, g_c are the evolving parameters. We consider g_a and g_c evolving on the intervals $[1.1 \times 10^{-12},\ 2.5 \times 10^{-12}]$ and $[0,\ 3.0 \times 10^{2}]$, respectively, and report in Fig.(11a) the size of the fourth band gap calculated against the prescribed g_a and g_c combinations. Similar to the previous case, we highlight four cases based on the combination of g_a and g_c, denoted by N, M, P, Q, and we plot in Fig.(11b) the corresponding band diagrams for the fourth band gap. If we only focus on the size of the band gap (Fig.(11a)), we note monotonically increasing trend with respect to g_a, however, the dependence on g_c is not monotonic. The size of the band gap first decreases, then increases with g_c, with the lowest point observed at $(g_a, g_c) = (1.1 \times 10^{-12}, 0)$. Position of the band gap is also influenced by g_a and g_c. By following the path N-M-Q-P, the lower bound of the band gap globally increases. Concerning dynamic response in frequency domain, we report the cases N, M, P, Q in Fig.(11c) on which the frequency range between the lowest and the highest bounds for the four cases combined, predicted by band gap calculation, is highlighted. It covers the fourth band gap that we can identify on the dynamic response curves.

The last case deals with DS control strategy for which $g_a = 0$ and g_b, g_c are set to evolve on the intervals $[0,\ 2.0 \times 10^{-5}]$ and $[0,\ 3.0 \times 10^{2}]$, respectively. We follow the same analysis methodology as for the two previous cases. In Fig.(12b), the size of the fourth band gap increases monotonically with g_c, yet the effect of g_b appears insignificant. We note in particular the cases P and Q, which presented comparable band gap sizes. We highlight in Fig.(12c) the frequency range covered by the highest and the lowest bounds predicted by unit cell band gap calculations. The highlighted frequency range does not suit perfectly but fully covers the fourth band gap that we can identify on the dynamic response curves.

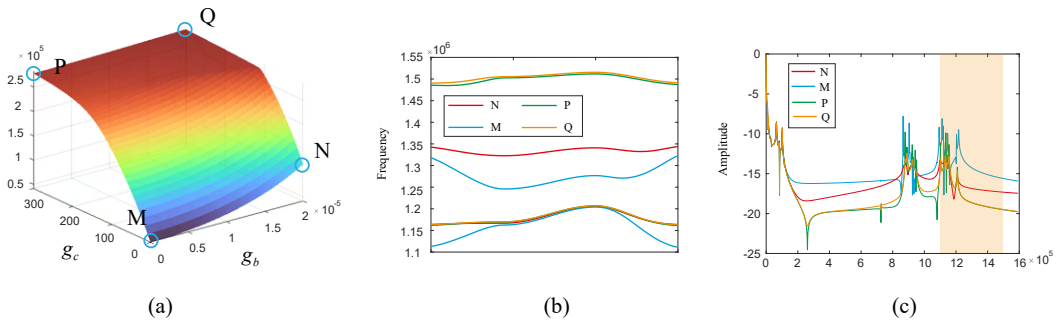

Figure 12: Effect of DS control: (a) Evolution of the fourth band gap size with respect to the combined effect of g_b and g_c simultaneously. (b) The fourth band gap diagrams considering cases N, M, P, Q. (c) Dynamic response in frequency domain based on a five unit cell couple micro plate system considering the cases N, M, P, Q.

In summary, the presented analysis allows evaluation of band gap effects for the implemented multi-parameter feedback control. The investigation led to quantitative relations that measure the collective effects of g_a, g_b and g_c combinations. We have observed that the collective effects of g_a, g_b and g_c cannot be predicted by considering direct superposition of their individual behaviours. In the case of MS control, for example, the fourth band gap is not a monotonic function with respect to g_c (Fig.(11a)) whereas it is the case when it comes to single-parameter control based on g_c as shown in Fig.(9a). In addition, setting of the MD, MS or DS control parameters affects both the band gap size and its position. The methodology involved in the current analysis can be used to obtain optimal parametrisation of the feedback controller with respect to the required band gap behaviour.

7 Conclusion

We investigated in this work a computational methodology that can be used to assist the design of feedback micro controllers for achieving tunable band gap properties of micro scale piezoelectric plate coupled systems. The methodology is based on a high-order elasto-dynamic model with piezoelectric coupling which accounts for size dependence of the vibroacoustic behaviours, and involves a feedback control relationship that incorporates three-parameter dependence with respect to displacement, velocity and acceleration (or stiffness, damping and mass in other terms). Effects of the three parameters on the band gap properties can be individually or collectively predicted by simulation, which allowed us to obtain an optimised parametrisation of the micro controller with respect to the design specifications. This is particularly interesting since according to our simulations, combined effects of the three control parameters cannot be predicted by considering linear superposition of their individual behaviours. For example, effects of the combined acceleration and displacement control (mass and stiffness or MS based control as described in Section 6.3) revealed significant difference compared to single-parameter strategies based on individual effects of acceleration or displacement alone, or on their superposition in any possible manner. Therefore, only through a comprehensive numerical methodology as the one developed in the present work, can we obtain an accurate prediction of the combined effects for the involved control parameters. Additionally, size dependence of band gap properties has been examined, which further confirms the value of this contribution on the topic of band gap tuning for micro scale plate coupled systems.

Appendix A

The matrix expression of linear elasticity tensor:

$$[\mathbf{C}] = \begin{bmatrix} C_{11} & C_{12} & 0 & 0 & 0 \\ C_{12} & C_{22} & 0 & 0 & 0 \\ 0 & 0 & C_{44} & 0 & 0 \\ 0 & 0 & 0 & C_{44} & 0 \\ 0 & 0 & 0 & 0 & \frac{C_{11}-C_{12}}{2} \end{bmatrix}.$$

The matrix expression of couple stress elasticity tensor:

$$[\mathbf{A}] = \begin{bmatrix} A_{11} & A_{12} & 0 & 0 & 0 \\ A_{12} & A_{22} & 0 & 0 & 0 \\ 0 & 0 & A_{44} & 0 & 0 \\ 0 & 0 & 0 & A_{44} & 0 \\ 0 & 0 & 0 & 0 & \frac{A_{11}-A_{12}}{2} \end{bmatrix},$$

where $A_{ij} = C_{ij}l^2$.

Appendix B

For Cauchy strain matrix:

$$\{\hat{\boldsymbol{\varepsilon}}\} = \begin{Bmatrix} \frac{\partial \phi_x}{\partial x} \\ \frac{\partial \phi_y}{\partial y} \\ \left(\frac{\partial \phi_x}{\partial y} + \frac{\partial \phi_y}{\partial x}\right) \\ \frac{\partial w}{\partial x} - \phi_x \\ \frac{\partial w}{\partial y} - \phi_y \end{Bmatrix} = \begin{bmatrix} 0 & \frac{\partial}{\partial x} & 0 \\ 0 & 0 & \frac{\partial}{\partial y} \\ 0 & \frac{\partial}{\partial y} & \frac{\partial}{\partial x} \\ \frac{\partial}{\partial x} & -1 & 0 \\ \frac{\partial}{\partial y} & 0 & -1 \end{bmatrix} \mathbf{N}\mathbf{u}^{(e)} = \mathbf{B}_\varepsilon \mathbf{u}^{(e)},$$

where

$$[\mathbf{B}_\varepsilon] = \begin{bmatrix} \mathbf{B}_{\varepsilon b} \\ \mathbf{B}_{\varepsilon s} \end{bmatrix} = \begin{bmatrix} 0 & \frac{\partial N_1}{\partial x} & 0 & 0 & \frac{\partial N_{1\xi}}{\partial x} & 0 & 0 & \frac{\partial N_{1\eta}}{\partial x} & 0 & \cdots \\ 0 & 0 & \frac{\partial N_1}{\partial y} & 0 & 0 & \frac{\partial N_{1\xi}}{\partial y} & 0 & 0 & \frac{\partial N_{1\eta}}{\partial y} & \cdots \\ 0 & \frac{\partial N_1}{\partial y} & \frac{\partial N_1}{\partial x} & 0 & \frac{\partial N_{1\xi}}{\partial y} & \frac{\partial N_{1\xi}}{\partial x} & 0 & \frac{\partial N_{1\eta}}{\partial y} & \frac{\partial N_{1\eta}}{\partial x} & \cdots \\ \frac{\partial N_1}{\partial x} & -N_1 & 0 & \frac{\partial N_{1\xi}}{\partial x} & -N_{1\xi} & 0 & \frac{\partial N_{1\eta}}{\partial x} & -N_{1\eta} & 0 & \cdots \\ \frac{\partial N_1}{\partial y} & 0 & -N_1 & \frac{\partial N_{1\xi}}{\partial y} & 0 & -N_{1\xi} & \frac{\partial N_{1\eta}}{\partial y} & 0 & -N_{1\eta} & \cdots \end{bmatrix}_{5\times 36}.$$

For symmetric curvature strain matrix:

$$\{\hat{\boldsymbol{\chi}}\} = \begin{pmatrix} \frac{\partial^2 w}{\partial y \partial x} + \frac{\partial \phi_y}{\partial x} \\ \frac{\partial^2 w}{\partial x \partial y} + \frac{\partial \phi_x}{\partial y} \\ \frac{\partial \phi_y}{\partial x} - \frac{\partial \phi_x}{\partial y} \\ \left(\frac{\partial^2 w}{\partial y^2} + \frac{\partial \phi_y}{\partial y}\right) - \left(\frac{\partial^2 w}{\partial x^2} + \frac{\partial \phi_x}{\partial x}\right) \\ \frac{\partial^2 \phi_y}{\partial x \partial y} - \frac{\partial^2 \phi_x}{\partial y^2} \\ \frac{\partial^2 \phi_y}{\partial x^2} - \frac{\partial^2 \phi_x}{\partial y \partial x} \end{pmatrix} = \begin{bmatrix} \frac{\partial^2}{\partial y \partial x} & 0 & \frac{\partial}{\partial x} \\ \frac{\partial^2}{\partial x \partial y} & \frac{\partial}{\partial y} & 0 \\ 0 & -\frac{\partial}{\partial y} & \frac{\partial}{\partial x} \\ \frac{\partial^2}{\partial y^2} - \frac{\partial^2}{\partial x^2} & -\frac{\partial}{\partial x} & \frac{\partial}{\partial y} \\ 0 & -\frac{\partial^2}{\partial y^2} & \frac{\partial^2}{\partial x \partial y} \\ 0 & -\frac{\partial^2}{\partial y \partial x} & \frac{\partial^2}{\partial x^2} \end{bmatrix} \mathbf{N}\mathbf{u}^{(e)} = \mathbf{B}_\chi \mathbf{u}^{(e)},$$

where

$$[\mathbf{B}_\chi] = \begin{bmatrix} \frac{\partial^2 N_1}{\partial x \partial y} & 0 & \frac{\partial N_1}{\partial x} & \frac{\partial^2 N_{1\xi}}{\partial x \partial y} & 0 & \frac{\partial N_{1\xi}}{\partial x} & \frac{\partial^2 N_{1\eta}}{\partial x \partial y} & 0 & \frac{\partial N_{1\eta}}{\partial x} & \cdots \\ \frac{\partial^2 N_1}{\partial y \partial x} & \frac{\partial N_1}{\partial y} & 0 & \frac{\partial^2 N_{1\xi}}{\partial y \partial x} & \frac{\partial N_{1\xi}}{\partial y} & 0 & \frac{\partial^2 N_{1\eta}}{\partial y \partial x} & \frac{\partial N_{1\eta}}{\partial y} & 0 & \cdots \\ 0 & -\frac{\partial^2 N_1}{\partial y^2} & \frac{\partial^2 N_1}{\partial x \partial y} & 0 & -\frac{\partial^2 N_{1\xi}}{\partial y^2} & \frac{\partial^2 N_{1\xi}}{\partial x \partial y} & 0 & -\frac{\partial^2 N_{1\eta}}{\partial y^2} & \frac{\partial^2 N_{1\eta}}{\partial x \partial y} & \cdots \\ 0 & -\frac{\partial^2 N_1}{\partial y^2} & \frac{\partial^2 N_1}{\partial x^2} & 0 & -\frac{\partial^2 N_{1\xi}}{\partial y \partial x} & \frac{\partial^2 N_{1\xi}}{\partial x^2} & 0 & -\frac{\partial^2 N_{1\eta}}{\partial y \partial x} & \frac{\partial^2 N_{1\eta}}{\partial x^2} & \cdots \\ \frac{\partial^2 N_1}{\partial y^2} - \frac{\partial^2 N_1}{\partial x^2} & -\frac{\partial N_1}{\partial x} & \frac{\partial N_1}{\partial y} & \frac{\partial^2 N_{1\xi}}{\partial y^2} - \frac{\partial^2 N_{1\xi}}{\partial x^2} & -\frac{\partial N_{1\xi}}{\partial x} & \frac{\partial N_{1\xi}}{\partial y} & \frac{\partial^2 N_{1\eta}}{\partial y^2} - \frac{\partial^2 N_{1\eta}}{\partial x^2} & -\frac{\partial N_{1\eta}}{\partial x} & \frac{\partial N_{1\eta}}{\partial y} & \cdots \end{bmatrix}_{5\times 36}.$$

Appendix C

For multi-layer piezoelectric plate:

$$\begin{aligned}
&[\mathbf{k}_{11}] = \textstyle\int_A [\mathbf{B}_\varepsilon]^T [\hat{\mathbf{C}}][\mathbf{B}_\varepsilon] \mathrm{d}A + \int_A [\mathbf{B}_\varepsilon]^T [\hat{\mathbf{C}}_{pa}][\mathbf{B}_\varepsilon] \mathrm{d}A + \int_A [\mathbf{B}_\varepsilon]^T [\hat{\mathbf{C}}_{ps}][\mathbf{B}_\varepsilon] \mathrm{d}A \\
&+ \textstyle\int_A [\mathbf{B}_\chi]^T [\hat{\mathbf{A}}_{pa}][\mathbf{B}_\chi] \mathrm{d}A + \int_A [\mathbf{B}_\chi]^T [\hat{\mathbf{A}}_{ps}][\mathbf{B}_\chi] \mathrm{d}A + \int_A [\mathbf{B}_\chi]^T [\hat{\mathbf{A}}][\mathbf{B}_\chi] \mathrm{d}A, \\
&[\mathbf{k}_{12}] = [\mathbf{k}_{21}]^T = -\textstyle\int_A [\mathbf{B}_\varepsilon]^T [\hat{\mathbf{e}}_a]^T [\mathbf{B}_{V_a}] \, \mathrm{d}A, \\
&[\mathbf{k}_{13}] = [\mathbf{k}_{31}]^T = -\textstyle\int_A [\mathbf{B}_\varepsilon]^T [\hat{\mathbf{e}}_s]^T [\mathbf{B}_{V_s}] \, \mathrm{d}A, \\
&[\mathbf{k}_{22}] = -\textstyle\int_A [\mathbf{B}_{V_a}]^T [\hat{\boldsymbol{\epsilon}}_a][\mathbf{B}_{V_a}] \mathrm{d}A, \\
&[\mathbf{k}_{33}] = -\textstyle\int_A [\mathbf{B}_{V_s}]^T [\hat{\boldsymbol{\epsilon}}_s][\mathbf{B}_{V_s}] \mathrm{d}A, \\
&[\mathbf{m}_{11}] = \textstyle\int_A [\mathbf{N}]^T [\boldsymbol{\rho}][\mathbf{N}] \mathrm{d}A,
\end{aligned}$$

with

$$\begin{aligned}
&[\hat{\mathbf{C}}] = \textstyle\int_{-\frac{h}{2}}^{\frac{h}{2}} [\mathbf{S}_\varepsilon]^T [\mathbf{C}][\mathbf{S}_\varepsilon] \mathrm{d}z, \\
&[\hat{\mathbf{C}}_{pa}] = \textstyle\int_{-\frac{h}{2}-h_p}^{-\frac{h}{2}} [\mathbf{S}_\varepsilon]^T [\mathbf{C}_p][\mathbf{S}_\varepsilon] \mathrm{d}z, \\
&[\hat{\mathbf{C}}_{ps}] = \textstyle\int_{\frac{h}{2}}^{\frac{h}{2}+h_p} [\mathbf{S}_\varepsilon]^T [\mathbf{C}_p][\mathbf{S}_\varepsilon] \mathrm{d}z, \\
&[\hat{\mathbf{e}}_a]^T = \textstyle\int_{-\frac{h}{2}-h_p}^{-\frac{h}{2}} [\mathbf{S}_\varepsilon]^T [\mathbf{e}]^T \mathrm{d}z, \\
&[\hat{\mathbf{e}}_s]^T = \textstyle\int_{\frac{h}{2}}^{\frac{h}{2}+h_p} [\mathbf{S}_\varepsilon]^T [\mathbf{e}]^T \mathrm{d}z, \\
&[\hat{\boldsymbol{\epsilon}}_a] = \textstyle\int_{-\frac{h}{2}-h_p}^{-\frac{h}{2}} [\boldsymbol{\epsilon}] \mathrm{d}z, \\
&[\hat{\boldsymbol{\epsilon}}_s] = \textstyle\int_{\frac{h}{2}}^{\frac{h}{2}+h_p} [\boldsymbol{\epsilon}] \mathrm{d}z, \\
&[\boldsymbol{\rho}] = \textstyle\int_{\frac{h}{2}}^{\frac{h}{2}+h_p} \begin{bmatrix} \rho & 0 & 0 \\ 0 & \rho z^2 & 0 \\ 0 & 0 & \rho z^2 \end{bmatrix} \mathrm{d}z.
\end{aligned}$$

For elastic plate:

$$\begin{aligned}
&[\mathbf{k}] = \textstyle\int_A [\mathbf{B}_\varepsilon]^T [\hat{\mathbf{C}}][\mathbf{B}_\varepsilon] dA + \int_A [\mathbf{B}_\chi]^T [\hat{\mathbf{A}}][\mathbf{B}_\chi] dA, \\
&[\mathbf{m}] = \textstyle\int_A [\mathbf{N}]^T [\rho][\mathbf{N}] \mathrm{d}A,
\end{aligned}$$

where

$$[\boldsymbol{\rho}] = \int_{-\frac{h}{2}}^{\frac{h}{2}} \begin{bmatrix} \rho & 0 & 0 \\ 0 & \rho z^2 & 0 \\ 0 & 0 & \rho z^2 \end{bmatrix} \mathrm{d}z.$$

References

[1] T. Naono, T. Fujii, M. Esashi, and S. Tanaka. A large-scan-angle piezoelectric MEMS optical scanner actuated by a Nb-doped PZT thin film. Journal of Micromechanics and Microengineering, 24(1):015010, 2013.

[2] K. Brueckner, F. Niebelschuetz, K. Tonisch, C. Foerster, V. Cimalla, R. Stephan, J. Pezoldt, T. Stauden, O. Ambacher, and M. Hein. Micro-and nano-electromechanical resonators based on SiC and group III-nitrides for sensor applications. physica status solidi (A), 208(2):357–376, 2011.

[3] J. Qu, J. Choi, and K. R. Oldham. Dynamics of millimeter-scale hexapod microrobotics with PZT-polymer micro-actuators. In 2017 IEEE International Conference on Advanced Intelligent Mechatronics (AIM), pages 1304–1309. IEEE, 2017.

[4] Y. Lu, H. Tang, Q. Wang, S. Fung, J. Tsai, M. Daneman, B. Boser, and D. Horsley. Waveguide piezoelectric micromachined ultrasonic transducer array for short-range pulse-echo imaging. Applied Physics Letters, 106(19):193506, 2015.

[5] T. Ren, C. Liu, F. Li, and C. Zhang. Active tunability of band gaps for a novel elastic metamaterial plate. Acta Mechanica, 231(10):4035–4053, 2020.

[6] B. Lossouarn, J.-F. Deü, M. Aucejo, and K. A. Cunefare. Multimodal vibration damping of a plate by piezoelectric coupling to its analogous electrical network. Smart Materials and Structures, 25(11):115042, October 2016.

[7] F. Li, C. Zhang, and C. Liu. Active tuning of vibration and wave propagation in elastic beams with periodically placed piezoelectric actuator/sensor pairs. Journal of Sound and Vibration, 393:14–29, 2017.

[8] A. Morel, G. Pillonnet, P. Gasnier, E. Lefeuvre, and A. Badel. Frequency tuning of piezoelectric energy harvesters thanks to a short-circuit synchronous electric charge extraction. Smart Materials and Structures, 28(2):025009, 2018.

[9] L. Chen, L. Chang, J. Xue, and H. Li. Experimental study of auto-tuning piezoelectric energy harvester attaching balls in boxes. EPL (Europhysics Letters), 130(5):54003, 2020.

[10] L. Yu, L. Tang, and T. Yang. Piezoelectric passive self-tuning energy harvester based on a beam-slider structure. Journal of Sound and Vibration, 489:115689, 2020.

[11] S. Yang, J. H. Page, Z. Liu, M. L. Cowan, C. T. Chan, and P. Sheng. Ultrasound tunneling through 3D phononic crystals. Physical Review Letters, 88(10):104301, 2002.

[12] J. Page. Focusing of ultrasonic waves by negative refraction in phononic crystals. AIP Advances, 6(12):121606, 2016.

[13] E. Walker, D. Reyes, M. M. Rojas, A. Krokhin, Z. Wang, and A. Neogi. Tunable ultrasonic phononic crystal controlled by infrared radiation. Applied Physics Letters, 105(14):143503, 2014.

[14] R. D. Mindlin. Microstructure in linear elasticity. Technical report, Columbia Univ New York Dept of Civil Engineering and Engineering Mechanics, 1963.

[15] D. C. Lam, F. Yang, A. Chong, J. Wang, and P. Tong. Experiments and theory in strain gradient elasticity. Journal of the Mechanics and Physics of Solids, 51(8):1477–1508, 2003.

[16] F. Yang, A. Chong, D. C. C. Lam, and P. Tong. Couple stress based strain gradient theory for elasticity. International Journal of Solids and Structures, 39(10):2731–2743, 2002.

[17] B. Zhang, Y. He, D. Liu, Z. Gan, and L. Shen. A non-classical mindlin plate finite element based on a modified couple stress theory. European Journal of Mechanics-A/Solids, 42:63–80, 2013.

[18] G. Zhang, X.-L. Gao, and S. Ding. Band gaps for wave propagation in 2-D periodic composite structures incorporating microstructure effects. Acta Mechanica, 229(10):4199–4214, 2018.

[19] Z.X. Xia, G.Y. Zhang, Y. Cong and S.T. Gu. A non-classical couple stress based Mindlin plate finite element framework for tuning band gaps of periodic composite micro plates. Journal of Sound and Vibration, 529:116889, 2022.

[20] F. Yang and Y. Rahmat-Samii. Microstrip antennas integrated with electromagnetic band-gap (EBG) structures: A low mutual coupling design for array applications. IEEE Transactions on Antennas and Propagation, 51(10):2936–2946, 2003.

[21] S. Krödel, N. Thomé, and C. Daraio. Wide band-gap seismic metastructures. Extreme Mechanics Letters, 4:111–117, 2015.

[22] Y.-Z. Wang, F.-M. Li, W.-H. Huang, and Y.-S. Wang. Effects of inclusion shapes on the band gaps in two-dimensional piezoelectric phononic crystals. Journal of Physics: Condensed Matter, 19(49):496204, 2007.

[23] G.-H. Li, Y.-Z. Wang, and Y.-S. Wang. Active control on switchable waveguide of elastic wave metamaterials with the 3d printing technology. Scientific reports, 9(1):1–8, 2019.

[24] W. Zhou, B. Wu, Muhammad, Q. Du, G. Huang, C. Lü, and W. Chen. Actively tunable transverse waves in soft membrane-type acoustic metamaterials. Journal of Applied Physics, 123(16):165304, 2018.

[25] V. Balamurugan and S. Narayanan. Shell finite element for smart piezoelectric composite plate/shell structures and its application to the study of active vibration control. Finite Elements in Analysis and Design, 37(9):713–738, 2001.

[26] O. C. Zienkiewicz and R. L. Taylor. The finite element method-solid mechanics. Butterworth Heinemann, 2000.

[27] H. M. Ma, X. L. Gao, and J. N. Reddy. A non-classical Mindlin plate model based on a modified couple stress theory. Acta Mechanica, 220(1-4):217–235, 2011.

[28] G. Zhang, Y. Qu, X.-L. Gao, and F. Jin. A transversely isotropic magneto-electro-elastic timoshenko beam model incorporating microstructure and foundation effects. Mechanics of Materials, 149:103412, 2020.

[29] R. D. Mindlin. Influence of Rotatory Inertia and Shear on Flexural Motions of Isotropic, Elastic Plates. Journal of Applied Mechanics, 18, 1951.